Bulletin of Geophysics and Oceanography Vol. 66, n. 1, pp. 73-94; March 2025
DOI 10.4430/bgo00479

Enhancement of the total horizontal gradient of potential field data using the Modified Gudermannian Function (*MGTHG*): application to aeromagnetic data from Georgia, USA

A. Alvandi, V.E. Ardestani and S.-H. Motavalli-Anbaran

Institute of Geophysics, University of Tehran, Tehran, Iran

(Received: 14 July 2024; accepted: 10 October 2024; published online: 28 January 2025)

ABSTRACT One of the primary goals in interpreting potential field data is to delineate the horizontal boundaries of subsurface geological structures. Edge detection in this context involves using various filters designed to identify edges through the directional gradients of the potential field. However, traditional filters often face challenges such as low resolution, false edge generation, and dependence on depth information. This study introduces an innovative filter that combines the total horizontal gradient with the modified Gudermannian function to enhance the accuracy and clarity in horizontal boundary detection. The effectiveness of this new filter is validated through the analysis of both synthetic data sets and a real case study from Georgia, USA. To reduce noise in both synthetic and real models, vertical gradients are calculated using the stable and effective α-vertical gradient ratio technique. The results indicate that the proposed filter successfully generates high-resolution pseudo-boundary maps and produces superior outcomes.

Key words: edge detection, modified Gudermannian function, potential field, Georgia.

1. Introduction

Edge enhancement techniques are pivotal in geophysical data analysis, particularly in the interpretation of potential field data such as gravity and magnetics. These methods aim to sharpen the boundaries and highlight the edges of subsurface geological structures, making them more distinct and easier to identify. By applying various filters and mathematical algorithms, edge enhancement techniques enhance the resolution of geophysical data, allowing for more accurate delineation of geological features that may otherwise be obscured or indistinct. These techniques are essential for applications used in mineral exploration, oil and gas prospecting, and environmental studies, that provide critical insights into the hidden complexities of the Earth's subsurface. In recent years, edge enhancement methods for gravity and magnetic data have been widely used to investigate subsurface structures, providing crucial insights into geological features that may not be easily discernible through conventional potential field interpretational techniques (Alvandi *et al.*, 2022a; Ai *et al.*, 2024). Edge detection filters are frequently employed in the interpretation of potential field anomalies to delineate regional-scale geological structures (e.g. Nabighian, 1984; Roest *et al.*, 1992; Fedi and Florio, 2001; Ekinci and Yigitbas, 2015; Pal *et al.*, 2016; Cooper, 2020; Deniz Toktay *et al.*, 2021a, 2021b; Eldosouky *et al.*, 2021; Narayan *et al.*, 2021; Alvandi *et al.*, 2022b; Sahoo *et al.*, 2022; Al-Bahadily *et al.*, 2023; Alvandi and Ardestani,

2023; Pham and Prasad, 2023; Ai *et al.*, 2024a; Alvandi and Motavalli-Anbaran, 2024; Deniz Toktay *et al.*, 2024).

However, traditional filters often face several significant challenges, including low resolution, which can obscure the fine details of the subsurface structures. This lack of clarity can lead to the misinterpretation of geological features. Additionally, these filters are prone to generating false edges, which can create misleading artefacts in the data and further complicate the interpretation process. Another critical limitation is given by their reliance on depth information, which can introduce inaccuracies, especially in areas with a complex geology. These issues underscore the need for advanced filtering techniques that can provide higher resolution, minimise false positives, and offer reliable detection of horizontal boundaries without being overly dependent on depth data. Addressing these challenges is crucial for improving the accuracy and effectiveness of potential field data analyses in geological studies (Eldosouky *et al.*, 2022; Prasad *et al.*, 2022a, 2022b, 2022c; Alvandi and Ardestani, 2023; Ai *et al.*, 2024b; Deniz Toktay *et al.*, 2024).

2. Edge detection filters

Cordell and Grauch (1985) identified horizontal boundaries by using the Total Horizontal Gradient (*THG*) method. In the *THG* filter, the horizontal boundaries of the potential field sources display the highest values. The *THG* can be expressed as follows:

$$THG = \sqrt{\left(\frac{\partial F}{\partial x}\right)^2 + \left(\frac{\partial F}{\partial y}\right)^2}. \quad (1)$$

The partial derivatives of the reduced-to-the-pole (RTP) magnetic and gravity data in the x- and y-directions are denoted as $\partial F/\partial x$ and $\partial F/\partial y$ in Eq. (1), in which F is the field function. A significant limitation of the *THG* filter is its weak delineation of deep boundaries (Saibi *et al.*, 2012; Prasad *et al.*, 2022c; Alvandi *et al.*, 2023a; Pham *et al.*, 2023; Deniz Toktay *et al.*, 2024). To address this issue, local phase filters or normalised filters have been developed. In this study, filters developed on the basis of the *THG* concept are presented.

One such filter is the Tilt Angle (*TA*), also known as the tilt derivative, which normalises the vertical derivative using horizontal derivatives. The *TA* can be expressed as follows (Miller and Singh, 1994):

$$TA = \tan^{-1}\left(\frac{\frac{\partial F}{\partial z}}{THG}\right). \quad (2)$$

In Eq. (2), $\partial F/\partial z$ represents the vertical gradient of the field. While the *TA* can detect anomalies at different depths, it does not provide distinct signals over horizontal boundaries (Eldosouky *et al.*, 2022).

Verduzco *et al.* (2004) demonstrated that employing the maximum amplitude of the *THG* of the *TA* (*THGTA*) is more effective and accurate in delineating horizontal boundaries compared to the *THG* and *TA* (Verduzco *et al.*, 2004). The *THGTA* is expressed as:

$$THGTA = \sqrt{\left(\frac{\partial TA}{\partial x}\right)^2 + \left(\frac{\partial TA}{\partial y}\right)^2}. \quad (3)$$

Cooper and Cowan (2006) introduced an improved version of the *THG* known as the normalised Total Horizontal Gradient (*TDX*) filter. This filter normalises the *THG* by using the vertical gradient and identifies the maxima along the horizontal boundaries of the body. The *TDX* is expressed as follows:

$$TDX = tan^{-1}\left(\frac{THG}{\left|\frac{\partial F}{\partial z}\right|}\right). \quad (4)$$

Additionally, Cooper and Cowan (2006) introduced another filter called the Hyperbolic Tilt Angle (*HTA*) procedure, as defined by Eq. (5), where the maximum amplitude aligns with the horizontal boundaries of the causative source. The *HTA* is expressed as follows:

$$HTA = R\left[tanh^{-1}\left(\frac{\frac{\partial F}{\partial z}}{THG}\right)\right]. \quad (5)$$

In Eq. (5), *R* denotes the real component of the hyperbolic tangent function.

Tatchum *et al.* (2011) proposed an improved version of the *THG* (*ITHG*) method, which integrates second-order gradients of gravity and magnetic data to improve the resolution of edge detection maps. The approach is calculated using the following relation:

$$ITHG = \sqrt{\left(\frac{\partial^2 F}{\partial z \partial x}\right)^2 + \left(\frac{\partial^2 F}{\partial z \partial y}\right)^2}, \quad (6)$$

where $\frac{\partial^2 F}{\partial z \partial x}$ and $\frac{\partial^2 F}{\partial z \partial x}$ are the vertical gradients of the potential field in the *x* and *y* directions. The maximum value of the *ITHG* represents the anomaly edges. Ferreira *et al.* (2013) proposed another filter to represent horizontal boundaries, referred to as the *TATHG*. This approach can be computed using the following formula:

$$TATHG = tan^{-1}\left[\frac{\frac{\partial THG}{\partial z}}{\sqrt{\left(\frac{\partial THG}{\partial x}\right)^2 + \left(\frac{\partial THG}{\partial y}\right)^2}}\right]. \quad (7)$$

In Eq. (7), $\frac{\partial THG}{\partial x}$, $\frac{\partial THG}{\partial y}$, and $\frac{\partial THG}{\partial z}$ are gradients of the *THG* in the directions *x*, *y*, and *z*, respectively. The *TATHG* delineates the demarcation between shallow and deep structures. Nevertheless, the resolution at the edges of the *TATHG* map is limited (Alvandi and Ardestani, 2023). To improve the resolution of edge detection maps, Ibraheem *et al.* (2023) introduced a filter that utilises user-defined parameters to produce clearer signals and enhance resolution. This filter,

known as the *THG* of the Modified Hyperbolic Tangent (*MTH*) function, can be expressed as follows:

$$THGMTH = \sqrt{\left(\frac{\partial MTH}{\partial x}\right)^2 + \left(\frac{\partial MTH}{\partial y}\right)^2} \tag{8}$$

where the *MTH* is given by:

$$MTH = tanh\left[\frac{M \times \frac{\partial^2 F}{\partial z^2}}{\sqrt{\left(\frac{\partial TDX}{\partial x}\right)^2 + \left(\frac{\partial TDX}{\partial y}\right)^2}}\right]. \tag{9}$$

In Eq. (9), $\frac{\partial TDX}{\partial x}$ and $\frac{\partial TDX}{\partial y}$ are horizontal derivatives of the *TDX*, $\frac{\partial^2 F}{\partial z^2}$ is the vertical derivative of the $\frac{\partial F}{\partial z}$, and *M* represents the average value of the gravity and magnetic fields. In Eq. (9), the Laplace relation is employed to compute $\frac{\partial^2 F}{\partial z^2}$ with the purpose of attenuating noise effect:

$$\frac{\partial^2 F}{\partial z^2} = \frac{-\partial^2 F}{\partial x^2} - \frac{\partial^2 F}{\partial y^2}. \tag{10}$$

Alvandi *et al.* (2023a) introduced the hyperbolic domain technique, also known as the Gudermannian Function (*GF*) technique. This approach is formulated using the *GF* and the second-order gradient of the field. The *GF* is defined as follows:

$$GF = 2tan^{-1}\left\{tanh\left[2\left(-M + \frac{\frac{\partial HHG}{\partial z}}{\sqrt{\left(\frac{\partial HHG}{\partial x}\right)^2 + \left(\frac{\partial HHG}{\partial y}\right)^2}}\right)\right]\right\}. \tag{11}$$

where

$$HHG = \left|\left(\frac{\partial^2 F}{\partial x \partial z}\right)^2 + \left(\frac{\partial^2 F}{\partial y \partial z}\right)^2\right|. \tag{12}$$

In Eq. (12), $\frac{\partial^2 F}{\partial x \partial z}$ and $\frac{\partial^2 F}{\partial y \partial z}$ are the horizontal gradients in the *z* direction. parameter *M* varies between 0.5 and 8, and its determination is subject to the interpreter's discretion. In order to facilitate a more effective comparison between the *GF* filter and its modified version, this study will analyse the minimum, recommended, and maximum *M* values as presented by Alvandi *et al.* (2023a).

3. The Modified Gudermannian Function (*MGTHG*)

This study introduces an advanced filter, with high-resolution capabilities, that leverages the Modified *GF* [*MGTHG*: Nayak and Pal (2019)] to delineate the horizontal boundaries of potential field sources across various depths. The *MGTHG* enhances the accuracy of boundary detection by refining the resolution of potential field data. The inverse tangent function, which shares similarities with the *MGTHG*, is frequently used for delineating horizontal boundaries in gravity and magnetic field data. This function plays a crucial role in several existing filters, including the *TA* filter (Miller and Singh, 1994), the *TDX* filter (Cooper and Cowan, 2006), the *TATHG* filter (Ferreira *et al.*, 2013), and the *GF* filter (Alvandi *et al.*, 2023a), among others. The primary foundation of the *MGTHG* method is based on research conducted by Ferreira *et al.* (2013). This technique combines the strengths of previous methods to provide improved resolution and more precise delineation of horizontal boundaries in potential field data. The filter is defined as:

$$MGTHG = \frac{2}{\pi} tan^{-1}\left\{ sinh\left[\frac{\frac{\partial THG}{\partial z} + \frac{\partial THG}{\partial z} - \sqrt{\left(\frac{\partial THG}{\partial x}\right)^2 + \left(\frac{\partial THG}{\partial y}\right)^2}}{\sqrt{\left(\frac{\partial THG}{\partial x}\right)^2 + \left(\frac{\partial THG}{\partial y}\right)^2}} \right] \right\}. \quad (13)$$

The primary goal of the proposed filter is to identify regions with abrupt changes in density or magnetisation. The peaks of the *MGTHG* filter effectively delineate the boundaries of anomalous bodies. The amplitude of the *MGTHG* ranges from -1 to +1 radians. A significant advantage of the *MGTHG* filter is its ability to precisely and sharply define boundaries. Unlike many new high-resolution filters, the resolution of the *MGTHG* results remains consistent and does not depend on user-selected parameters (Prasad *et al.*, 2022a, 2022b; Alvandi and Ardestani, 2023; Alvandi *et al.*, 2023a, 2023b; Ibraheem *et al.*, 2023; Pham, 2023).

4. Mitigating the effect of noise

Horizontal gradients are calculated in the spatial domain through the application of finite difference methods (Ekinci *et al.*, 2013, 2020). This study utilises the α-Vertical Gradient Ratio (αVGR) technique to compute vertical gradients, employing a finite difference formula to mitigate the effects of noise (Oliveira and Pham, 2022).

$$\frac{\partial THG}{\partial z} = \frac{e_1 THG(h_1) + e_2 THG(h_2) + e_3 THG(h_3) + e_4 THG(h_4) + e_5 THG(h_5)}{\Delta h} \quad (14)$$

where e_1, …, e_5 are provided by:

$$
\begin{aligned}
e_1 &= \left(2\alpha^3+15\alpha^2+35\alpha+25\right)/12\\
e_2 &= \left(-8\alpha^3-54\alpha^2-104\alpha-48\right)/12\\
e_3 &= \left(12\alpha^3+72\alpha^2+114\alpha+36\right)/12\\
e_4 &= \left(-8\alpha^3-42\alpha^2-56\alpha-16\right)/12\\
e_5 &= \left(2\alpha^3+9\alpha^2+11\alpha+3\right)/12.
\end{aligned}
\tag{15}
$$

Moreover, $THG(h_i)$ is the data upward continued to $h_i=d_0-\alpha\,\Delta h-(i-1)\,\Delta h$ for $1\le i\le 5$, and d_0 is the observation plane height. In this case, we followed the recommendation of Oliveira and Pham (2022) and used α=30 and Δh=0.1 of grid spacing. Refer to Oliveira and Pham (2022) for more details of the αVGR method.

In the following sections, the efficacy of the proposed filter will be evaluated by comparing its outcomes with those achieved by other filters, including *THG* (Cordell and Grauch, 1985), *TA* (Miller and Singh, 1994), *THGTA* (Verduzco *et al.*, 2004), *TDX* (Cooper and Cowan, 2006), *HTA* (Cooper and Cowan, 2006), *ITHG* (Tatchum *et al.*, 2011), *TATHG* (Ferreira *et al.*, 2013), *THGMTH* (Ibraheem *et al.*, 2023), and *GF* (Alvandi *et al.*, 2023a). Additionally, the *GF* is configured with a minimum value of 0.5, a proposed value of 1.5, and a maximum value of 8 (Alvandi *et al.*, 2023a). The kernel of the proposed filter is based on the *THG*. Consequently, the previously discussed filters are introduced to facilitate comparison and demonstrate the effectiveness of the newly proposed technique.

5. Application on synthetic models

The effectiveness of the proposed approach, along with other edge detection methods, is assessed through the analysis of synthetic magnetic and gravity data under various conditions, including both noisy and noise-free scenarios. The first scenario involves a model with four buried sources, illustrated in both perspective and plan views in Figs. 1a and 1b. The gravity anomalies of these prisms were calculated using the algorithm developed by Rao *et al.* (1990), with observation points spaced 1 km apart over a 251×251 km^2 area, as shown in Fig. 1c, and the synthetic anomaly with 3% added Gaussian noise is represented in Fig. 1d. The detailed description of the parameters attributed to the buried bodies is presented in Table 1.

Table 1 - Geometric parameters and designations of the synthetic gravity sources.

Parameters/Label	G1	G2	G3	G4
The centre *x* coordinate (km)	50	125	200	125
The centre *y* coordinate (km)	50	125	200	125
The prism width (km)	50	80	50	30
The prism length (km)	50	80	50	30
Depth to the top of the prism (km)	4	3	1	2
Depth to the bottom of the prism (km)	5.5	4	2.5	2.5
Density contrast (g/cm^3)	0.5	-0.8	0.5	0.8
Strike azimuth (degree)	0	0	0	90

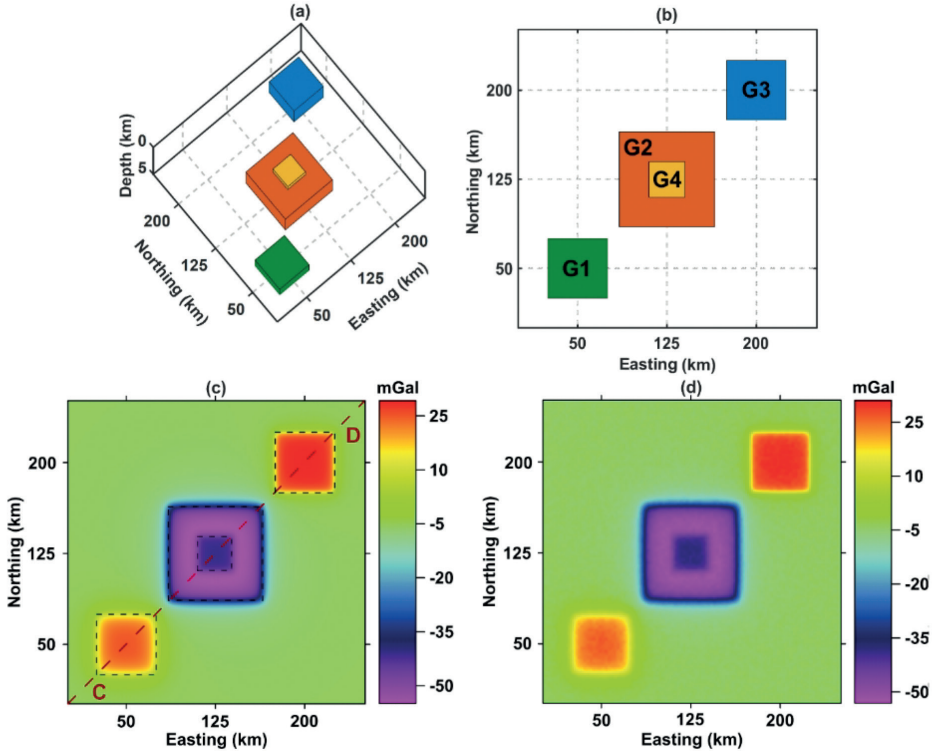

Fig. 1 - a) The gravity model in three dimensions (3D); b) plan view; c) corresponding gravity anomaly; d) noisy gravity anomaly. In panel c, the dashed red line represents profile C-D across the synthetic gravity model, while the dashed black lines indicate the actual horizontal boundaries.

5.1. Gravity model (without noise)

Fig. 2a shows the boundaries detected using the *THG* technique on the anomaly depicted in Fig. 1c. The results highlight that the large-amplitude responses from shallow source G3 significantly impact the *THG*, making its boundaries more pronounced, whereas the boundaries of the deeper source are notably less defined. The boundary of source G4 also appears blurred compared to source G2, which is attributed to its smaller amplitude. Fig. 2b presents the *TA* map for the gravimetric anomaly. The *TA* detector has limitations in accurately defining horizontal boundaries, resulting in spurious edge information around source G2 and within source G4. Fig. 2c illustrates the boundaries detected with the *THGTA* filter. This method clearly outlines the boundaries of two shallow sources but shows blurred edges for deeper sources. It also introduces some false borders. Fig. 2d shows the edge detection results using the *TDX* detector. While this method effectively outlines all edges, it tends to produce broad boundaries for source G4 and some spurious edge information near other sources. Fig. 2e depicts the edges identified by the *HTA* detector. The boundaries are faint, with visible spurious edges in the resulting image. Fig. 2f illustrates the results from the *ITHG* filter. The boundaries of source G3 is well defined, but the edges of sources G1, G2, and G4 appear blurred. Fig. 2g presents the results of the *TATHG* filter. Although it can simultaneously map edges at various depths, the resolution of the resulting edge image is relatively low. Fig. 2h displays the boundaries identified by the *THGMTH* detector. This method provides a clear representation of boundaries but also generates spurious and false borders around sources G1, G2, and G3. Figs. 2i, 2j, and 2k illustrate the boundaries delineated

using the *GF* technique with *M* values of 0.5, 1.5, and 8, respectively. Although the *GF* method provides a high-resolution representation of boundaries, it also produces spurious borders surrounding source G3 and results in a faint or poorly defined boundary for other sources. As parameter *M* increases, the borders become fainter, and no edge is delineated for G1. Fig. 2l illustrates the boundaries identified using the *MGTHG* technique, which, by providing high-resolution detection of all edges without generating false boundaries, offers a distinct advantage over the *THGMTH*, *GF*, and *TATHG* methods. To further clarify the effectiveness of the proposed method, a two dimensional cross-section was created.

Fig. 3a presents the gravity data along the C-D profile, while Figs. 3b to 3m display various representations, including *THG*, *TA*, *THGTA*, *TDX*, *HTA*, *ITHG*, *TATHG*, *THGMTH*, *GF* (*M*=0.5), *GF* (*M*=1.5), *GF* (*M*=8), and *MGTHG*. In the *GF* method, an increase from 0.5 to 8 in the *M* parameter results in the elimination of false boundaries. However, the boundaries of other structures either remain unrepresented or are depicted with diminished clarity. Notably, the *MGTHG* method

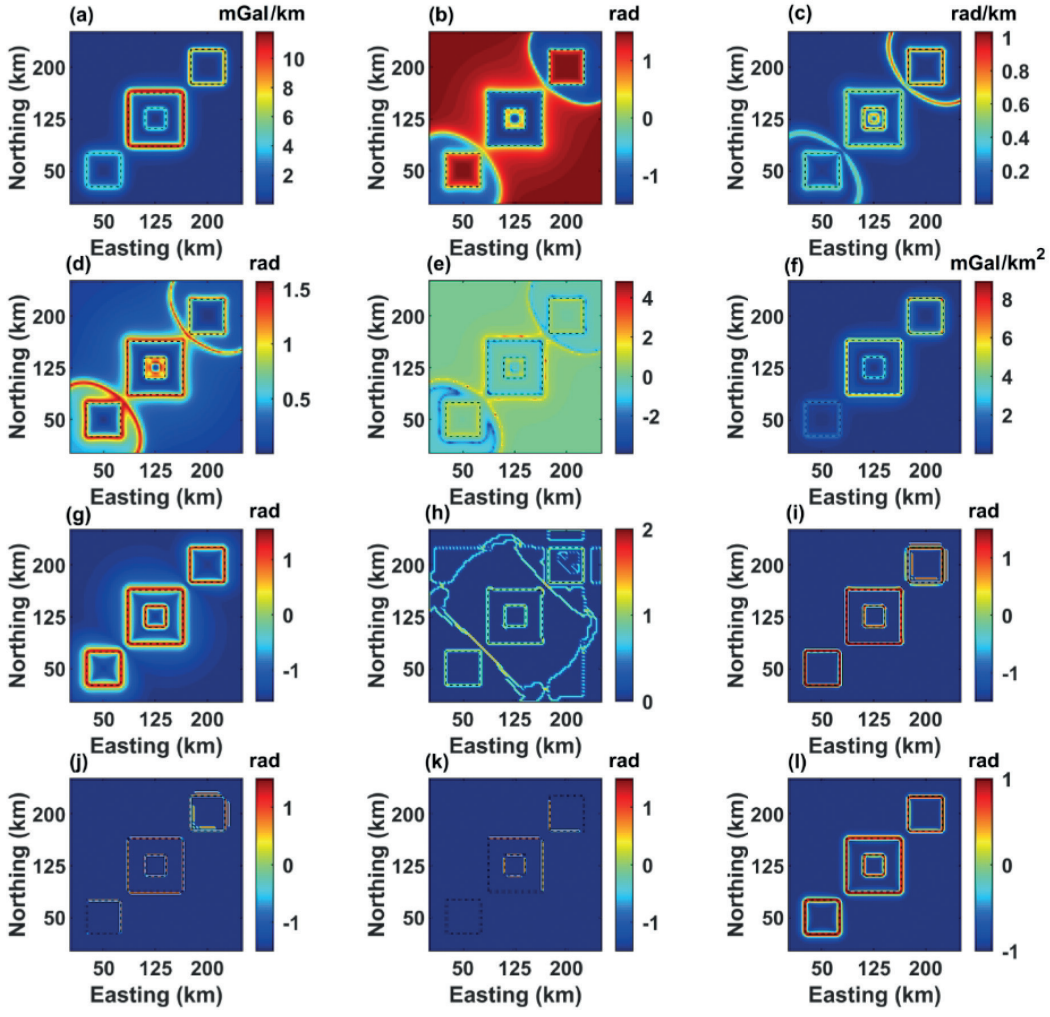

Fig. 2 - Horizontal boundaries were determined by mapping the data in Fig. 1c: a) *THG*; b) *TA*; c) *THGTA*; d) *TDX*; e) *HTA*; f) *ITHG*; g) *TATHG*; h) *THGMTH*; i) *GF* (*M*=0.5); j) *GF* (*M*=1.5); k) *GF* (*M*=8); and l) *MGTHG* (the actual boundaries are indicated with dashed black lines).

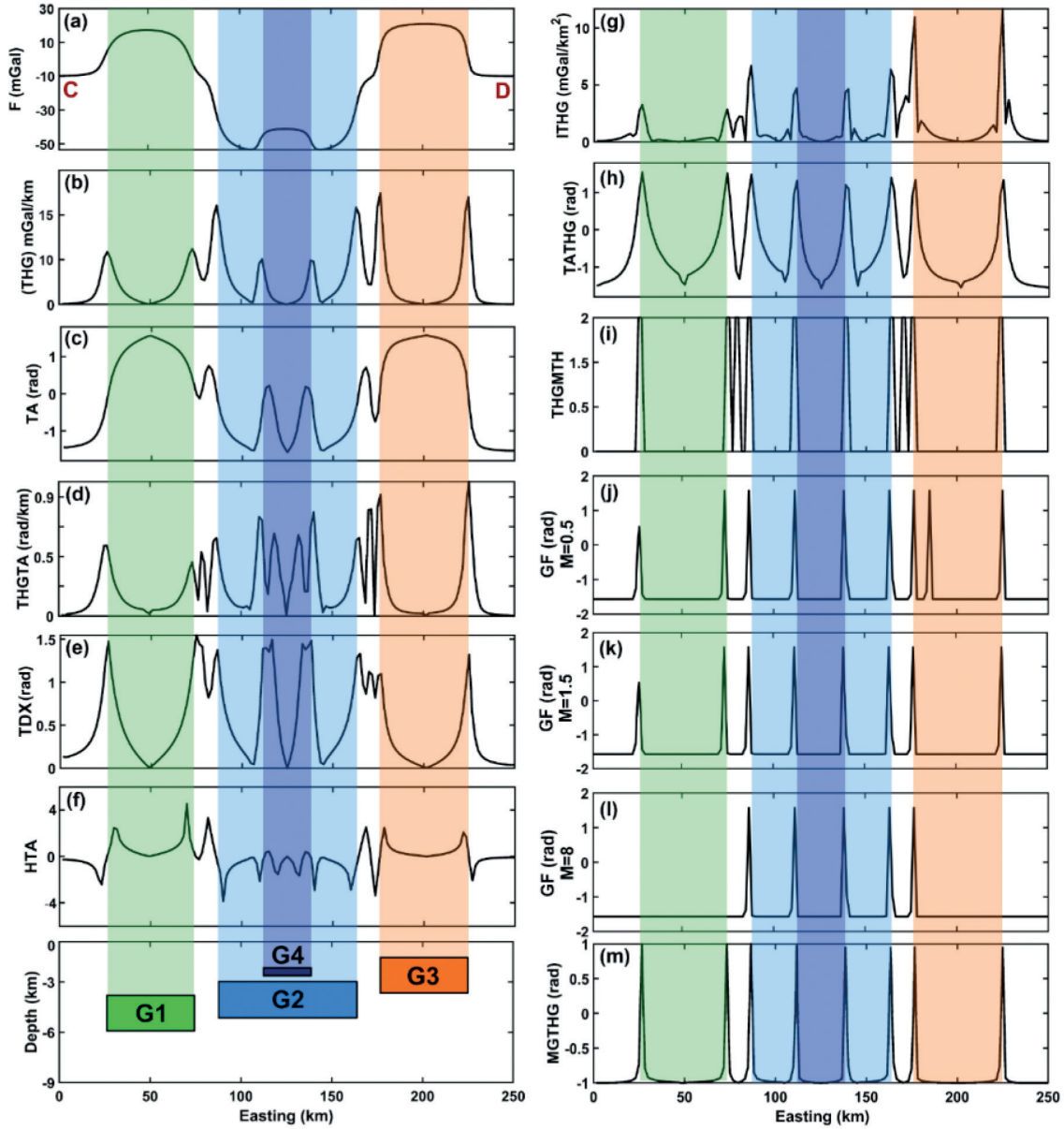

Fig. 3 - Two dimensional cross section (Fig. 1c) constructed from the model: a) gravity anomaly; b) *THG*; c) *TA*; d) *THGTA*; e) *TDX*; f) *HTA*; g) *ITHG*; h) *TATHG*; i) *THGMTH*; j) *GF* (*M*=0.5); k) *GF* (*M*=1.5); l) *GF* (*M*=8); and m) *MGTHG*.

exhibits enhanced resolution in mapping all boundaries when compared to alternative techniques and effectively avoids the generation of false boundaries both within and surrounding the buried bodies.

5.2. Gravity model (with noise)

In the second scenario, the sensitivity of the detectors to Gaussian noise was assessed by evaluating their response to the noisy anomaly shown in Fig. 1d. This noise, with an amplitude of

3% of the anomaly amplitude, was added to the anomalies in Fig. 1c. The horizontal boundaries identified by various detectors, including *THG, TA, THGTA, TDX, HTA, ITHG, TATHG, THGMTH, GF* (*M*=0.5, *M*=1.5, and *M*=8), and *MGTHG*, are illustrated in Figs. 4a to 4l. The *THG* detector, based on horizontal gradients, shows decreased susceptibility to noisy data compared to other detectors. However, it is still affected by the shallow anomalies associated with structure G1 (Fig. 4a). Fig. 4b presents anomalies computed using the *TA* detector. While the *TA* detector provides a balanced image for all sources, it introduces artefacts around source G2 and within source G4. The effectiveness of the *THGTA* detector is reduced when delineating the boundaries of sources G1, G2, G3, and G4, with the edges in the *THGTA* map exhibiting significant blurring, as shown in Fig. 4c. Fig. 4d illustrates the edges generated by the *TDX* approach. This method effectively produces balanced images of the source edges; however, the boundaries in the *TDX* map appear diffuse,

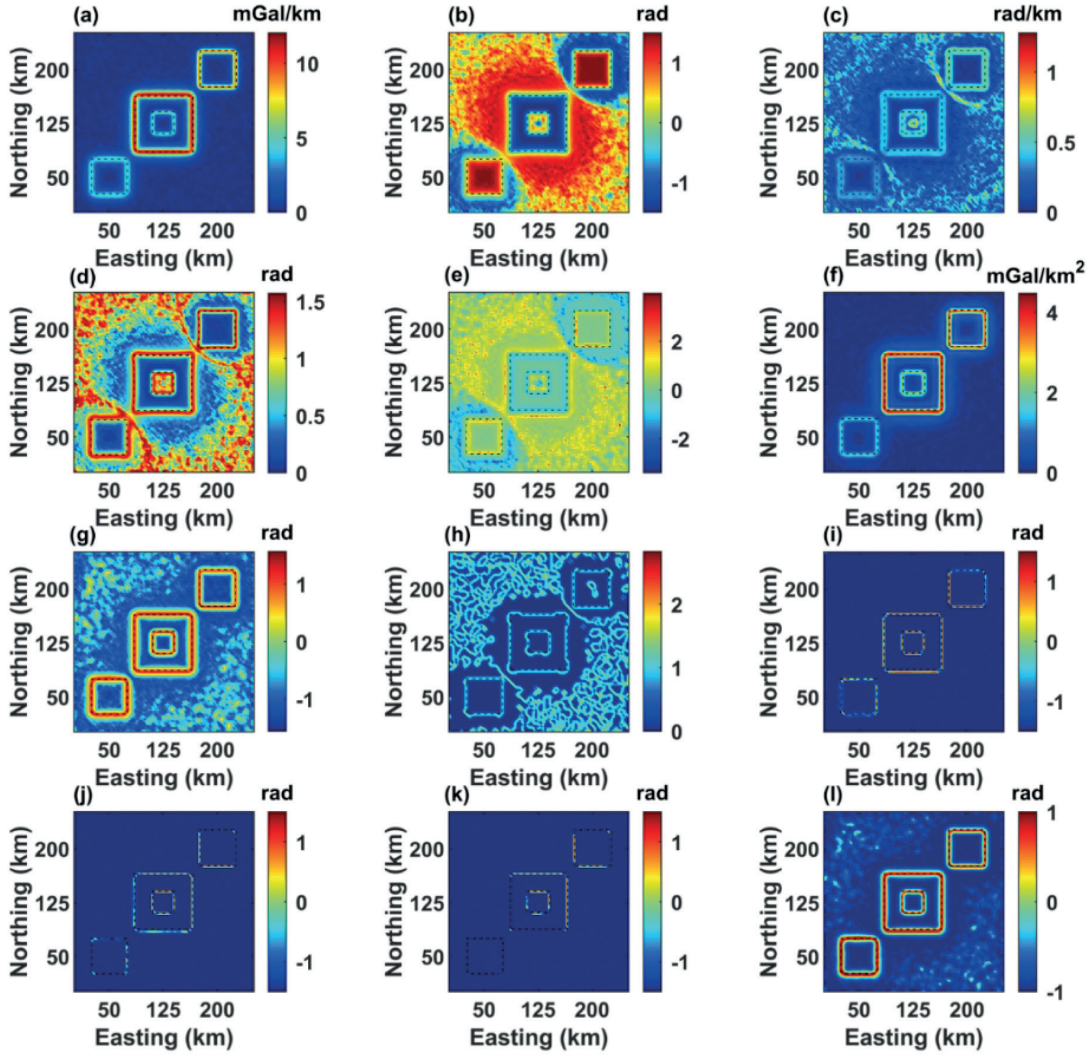

Fig. 4 - Horizontal boundary determination maps of data in Fig. 1d: a) *THG*; b) *TA*; c) *THGTA*; d) *TDX*; e) *HTA*; f) *ITHG*; g) *TATHG*; h) *THGMTH*; i) *GF* (*M*=0.5); j) *GF* (*M*=1.5); k) *GF* (*M*=8); and l) *MGTHG* (the actual boundaries are indicated with dashed black lines).

leading to the generation of false borders around structures G1, G2, and G3, as well as within source G4. Fig. 4e shows the boundaries identified using the *HTA* method. The detector faintly delineates the boundaries of sources G1, G2, and G3, while omitting the boundary of G4. Fig. 4f presents the results of the *ITHG* analysis, demonstrating that the large signals from the shallow body G1 dominate the *ITHG* map, causing the boundaries of the deeper bodies to appear blurred. Fig. 4g shows the edges extracted using the *TATHG* method, which creates balanced boundaries for buried sources; yet, the horizontal boundaries in the *TATHG* map appear diffuse. Fig. 4h displays anomalies detected by the *THGMTH* detector, which, using second-order vertical data derivatives, is more noise-sensitive than other detectors. Although this method outlines the borders of buried sources, the map contains numerous false and inaccurate borders. Figs. 4i, 4j, and 4k illustrate the boundaries identified using the *GF* method, which provides a clear output with high resolution. However, the borders of sources G1, G2, and G3 are not fully represented. Fig. 4l illustrates the edges identified by the proposed *MGTHG* detector. Notably, the *MGTHG* detector effectively detects all edges even in the presence of noise, without producing false edges around or above the sources. In this scenario, the *MGTHG* detector consistently produces high-resolution edge images.

5.3. Magnetic model (without noise)

In the third scenario, a magnetic anomaly pattern comprising 10 prisms was considered. The characteristics of these sources are detailed in Table 2. Fig. 5a presents a perspective view of the structures, while Fig. 5b shows the plan view of the sources. Additionally, Fig. 5c illustrates the magnetic effects produced by these sources, calculated on a square grid with a cell size of 1×1 km^2. Observations were collected over an area of 251×251 km^2 using the algorithm proposed by Rao and Babu (1991). The detectors used in the synthetic gravity example were also employed in this scenario.

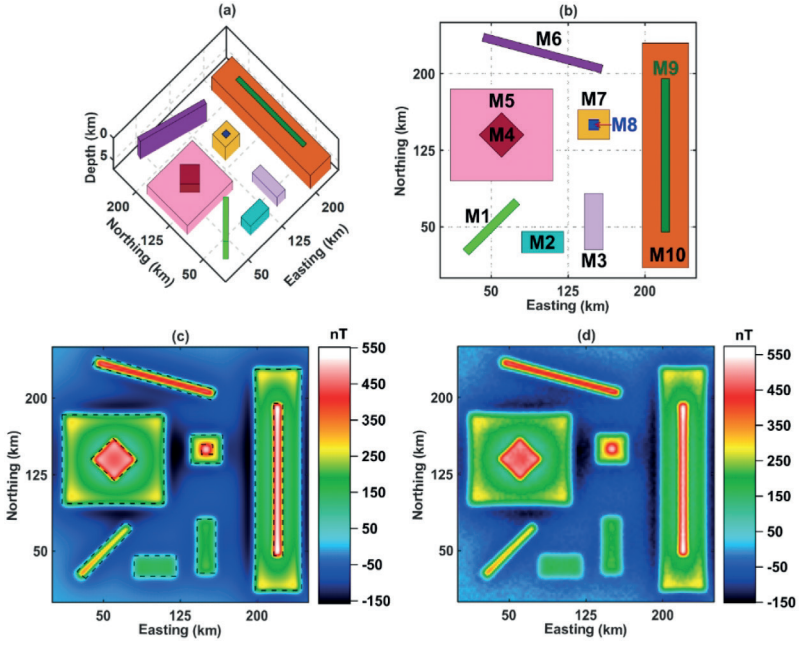

Fig. 5 - a) The magnetic model in 3D; b) plan view; c) corresponding magnetic anomaly; and d) noisy magnetic anomaly (the actual horizontal boundaries are represented with dashed black lines in panel c).

Table 2 - Geometric parameters and designations of the synthetic magnetic sources.

Parameters/Label	M1	M2	M3	M4	M5	M6	M7	M8	M9	M10
The centre *x* coordinate (km)	50	100	150	60	60	100	150	150	220	220
The centre *y* coordinate (km)	50	35	55	140	140	220	150	150	120	120
The prism width (km)	70	21	18	31	100	120	10	31	8	45
The prism length (km)	8	41	55	31	90	8	10	29	150	220
Depth to the top of the prism (km)	3	5	5	3	5	3	4	4	3	4
Depth to the bottom of the prism (km)	8	8	8.5	8	11	9.5	7	10	7.5	9
Magnetisation (A/m)	-1.35	1.30	-1.25	-1.40	1.30	-1.30	-1.25	-1.45	1.25	-1.30
Strike azimuth (degree)	-45	90	0	45	0	15	0	0	0	0

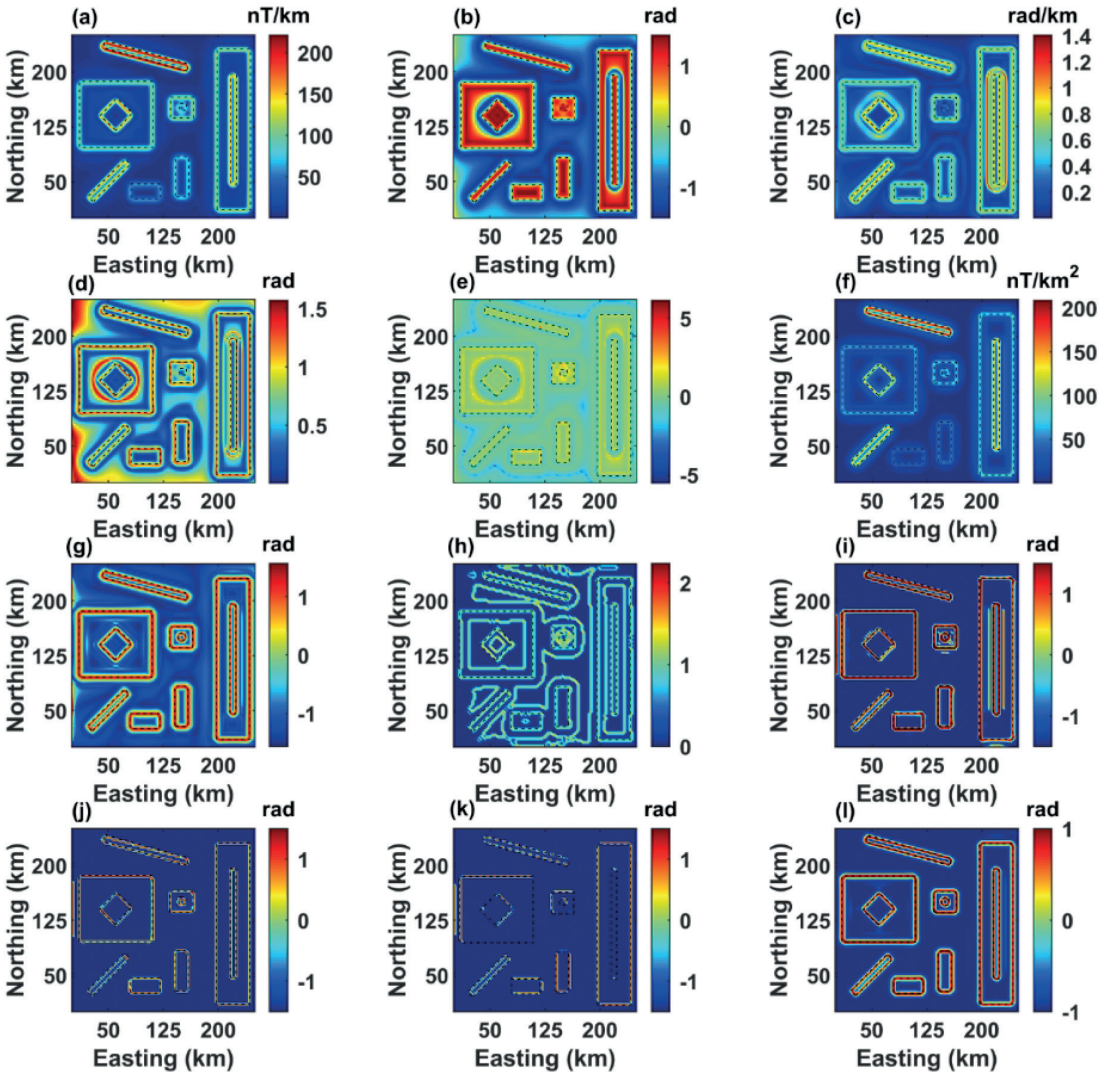

Fig. 6 - Horizontal boundary determination maps of data in Fig. 5c: a) *THG*; b) *TA*; c) *THGTA*; d) *TDX*; e) *HTA*; f) *ITHG*; g) *TATHG*; h) *THGMTH*; i) *GF* (*M*=0.5); j) *GF* (*M*=1.5); k) *GF* (*M*=8); and l) *MGTHG* (the actual boundaries are indicated with dashed black lines).

Fig. 6a displays the outcomes obtained from the *THG* technique. The analysis shows that the predominant signals associated with sources M1, M4, M6, and M9 are prevalent in the results of both approaches, while the delineations of the other sources appear blurred. Fig. 6b displays the boundary map generated using the *TA* approach. In this representation, the boundary of source M8 is not drawn, and false edges are observed in the delineation of the boundaries surrounding sources M4 and M9. Fig. 6c illustrates the *THGTA* map. This filter proves to be insufficient in effectively balancing signals originating from different sources at varying depths. Similarly, to the previous case, the edge determination map exhibits a blurred appearance. Fig. 6d shows the boundaries determined by applying the *TDX* detector to the magnetic data in Fig. 5c. Although this method can map all source boundaries, it generates false edge information between or around sources M1, M2, M3, and M6, resulting in diffuse borders. Additionally, the border of the M8 source has not been depicted. Fig. 6e depicts the results of edge detection employing the *HTA* filter. The boundaries of structures M2, M3, and M8 exhibit indistinctness, while other structures remain unresolved. Additionally, a spurious border is delineated around sources M4 and M9. Fig. 6f illustrates the boundary delineated by *ITHG*. In this case, the efficacy of this filter is unsatisfactory. While the boundaries of sources M1, M4, M6, and M9 are distinctly outlined, the depiction of the other sources appears blurred. Fig. 6g presents the boundaries calculated using the *TATHG* detector, which can simultaneously map boundaries at different depths. Despite its effectiveness in mapping all boundaries, the edge image resulting from the *TATHG* has low resolution. Fig. 6h illustrates the boundaries identified through the application of the *THGMTH* detector to the magnetic data depicted in Fig. 5c. The figure demonstrates that, although the *THGMTH* method produces a high-resolution representation of the boundaries, it also introduces spurious borders between and around all buried sources. Fig. 6i illustrates the edge determination map generated using the *GF* filter with a parameter value of M=0.5. This map effectively highlights the horizontal edges of all buried sources. However, false edges are detected on the left side of source M5 and around sources M4, M7, M8, and M9. Fig. 6j presents the edge determination map using the *GF* filter with M=1.5, which also highlights the horizontal edges of all buried sources. Nonetheless, a false edge is detected on the left side of source M5. Ultimately, Fig. 6k shows the edge determination map using the *GF* filter with M=8. This filter exhibits significant limitations in accurately delineating the boundaries of the causative bodies, resulting in a weak representation of their edges. Fig. 6l presents the edges detected by the *MGTHG* filter. Similarly to the *GF* filter, the *MGTHG* filter provides higher resolution boundaries compared to the other detectors. However, unlike the *GF*, the *MGTHG* method can map all body boundaries without introducing false edges.

5.4. Magnetic model (with noise)

In the fourth scenario, an analysis was conducted to assess the sensitivity of the proposed detectors and that of others to noise (Fig. 5d). This noise is of Gaussian type, with an amplitude of 3% of the anomaly amplitude from the anomalies in Fig. 5c.

Fig. 7a depicts the delineated boundaries derived from the *THG* detector. The *THG* detector utilises horizontal gradients of magnetic data, which makes it less susceptible to noise compared to other detectors, as reported by Saibi *et al.* (2019). Nevertheless, this detector remains significantly affected by the large signals from shallow sources M1, M4, M6, and M9. Fig. 7b illustrates the outcomes of edge detection employing the *TA* filter. The horizontal boundary of source M8 appears indistinct, and spurious boundaries are delineated around sources M4 and M9. In Fig. 7c, the *THGTA* filter exhibits limitations in accurately detecting the horizontal

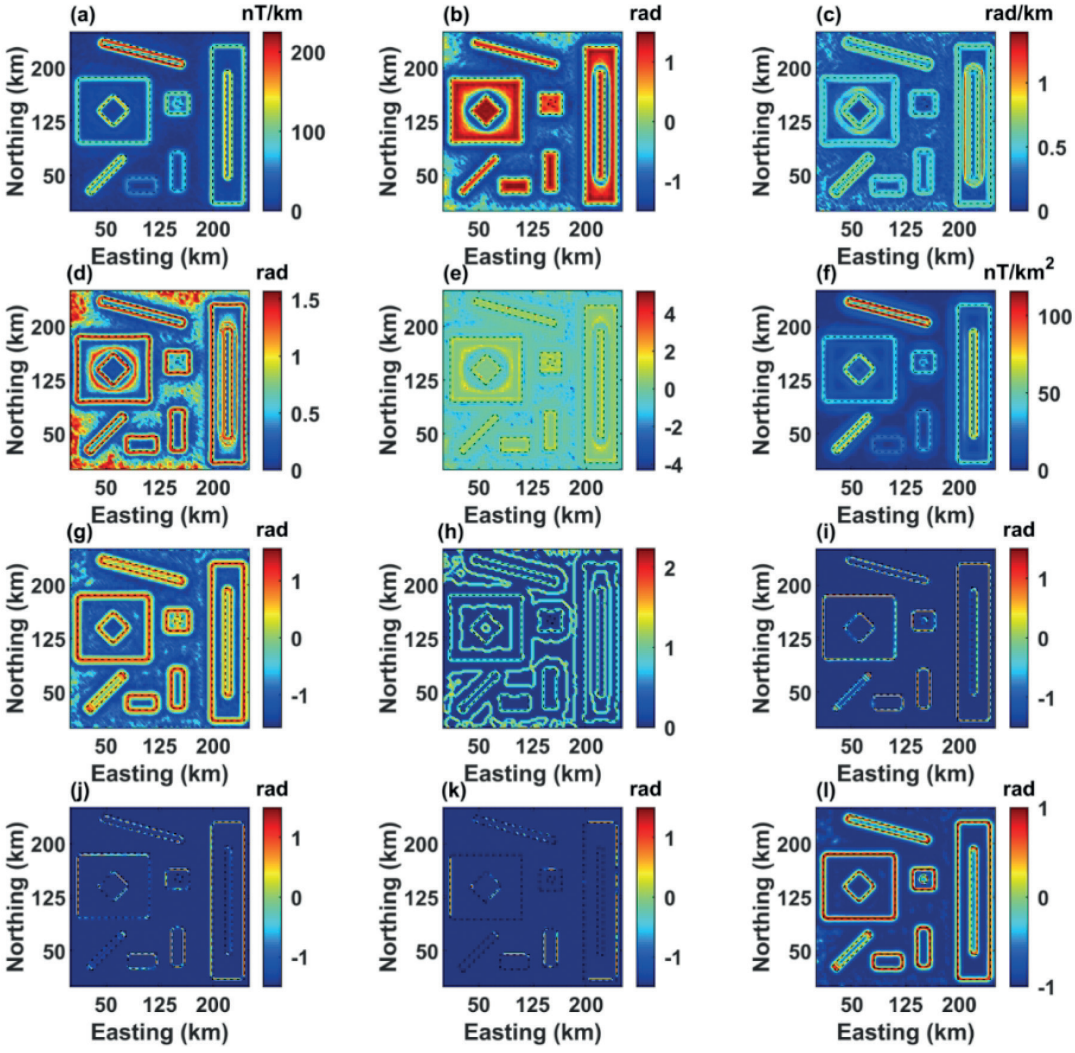

Fig. 7 - Horizontal boundary determination maps of data in Fig. 5d: a) *THG*; b) *TA*; c) *THGTA*; d) *TDX*; e) *HTA*; f) *ITHG*; g) *TATHG*; h) *THGMTH*; i) *GF* (*M*=0.5); j) *GF* (*M*=1.5); k) *GF* (*M*=8); and l) *MGTHG* (the actual boundaries are indicated with dashed black lines).

boundaries of buried sources. It lacks the capability to differentiate between the horizontal boundaries of sources at varying depths, resulting in inaccuracies in border mapping and in the production of a blurred map. Fig. 7d illustrates the outcomes of edge determination utilising the *TDX* filter. The map does not depict the edge of source M8 and displays false borders that may lead to misinterpretation. Fig. 7e illustrates the outcomes of edge detection using the *HTA* filter, where the horizontal boundaries of the sources appear faint, and spurious and supplementary borders are observable on the map. Fig. 7f demonstrates the results of edge detection utilising the *ITHG* filter. The map clearly shows the horizontal boundary of source M6, while the boundaries of other sources appear blurred and indistinct. Fig. 7g illustrates the boundaries identified by the *TATHG* detector. This filter showcases its capability to accurately detect all body edges without producing false boundaries. However, the *TATHG* map displays a diffuse appearance. Figs. 7h, 7i, 7j, and 7k depict the boundaries obtained from the *THGMTH* and *GF* methods. The

illustrations indicate that these techniques are more susceptible to noise compared to others. This susceptibility can be attributed to the fact that the *THGMTH* and *GF* detectors rely on the second vertical derivative of the magnetic data. Fig. 7l illustrates the edges detected using the *MGTHG* technique introduced in this research. The proposed detector demonstrates the ability to accurately detect all edges, even in the presence of noise, while avoiding the generation of false edges around or above the sources. The *MGTHG* consistently generates high-resolution edge images in this scenario.

6. Application on aeromagnetic data

The practical applicability of the proposed filter is demonstrated through the analysis of high-resolution aeromagnetic data from a region in Georgia, USA. The study area, spanning longitudes 82.80° W to 84.30° W and latitudes 32.20° N to 34.50° N, encompasses two distinct geological regions: the piedmont and the coastal plain. The fall line (FL) marks the boundary between these regions (Fig. 8). The piedmont region is characterised by igneous and metamorphic rocks such as schist, amphibolite, gneiss, and granite (Hack, 1982). In contrast, the coastal plain consists of sedimentary rocks deposited from the Late Cretaceous to the Holocene periods. A simplified geologic map of the area, adapted from Lawton *et al.* (1976) and Pickering and Murray (1976), is shown in Fig. 8 at a scale of 1:500,000. The use of regional aero-radioactivity, aeromagnetic

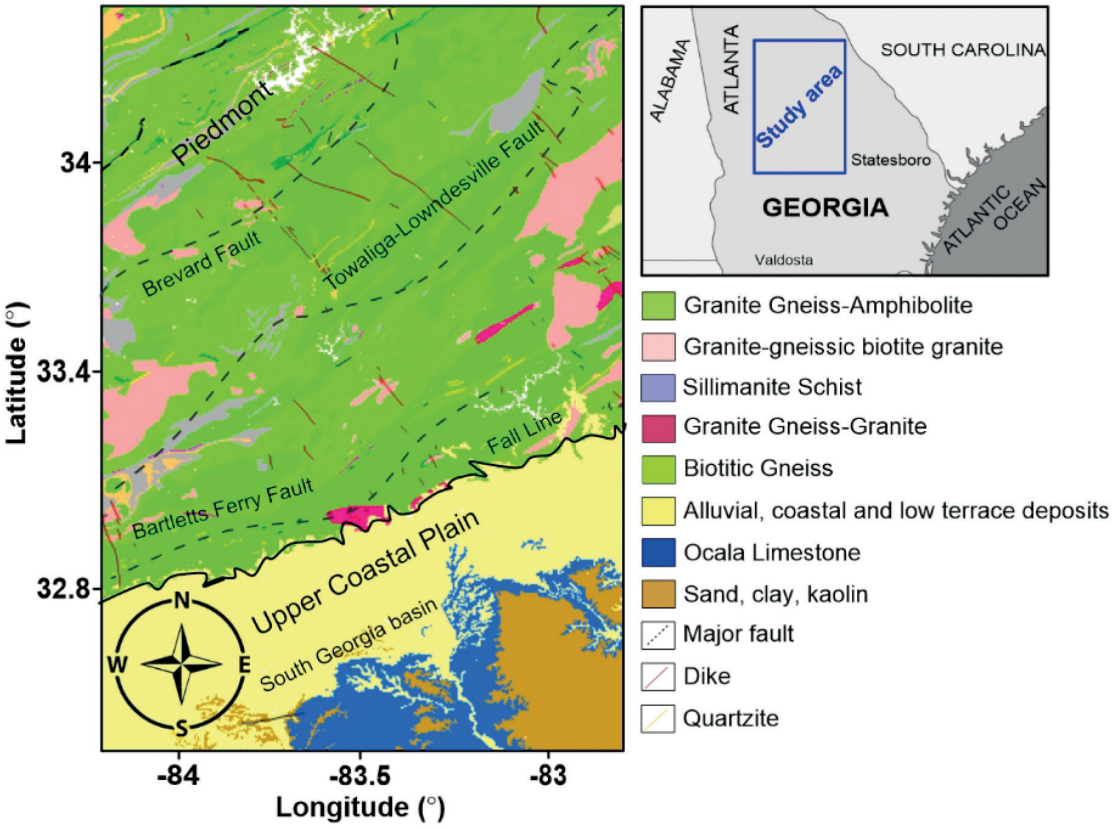

Fig. 8 - The simplified geological location and map of the study area.

mapping, and seismic reflection studies in Georgia, has helped determine fault and dike locations (Bentley *et al.*, 1974; Daniels, 1974, 2001; Alarifi, 2022). This approach has proven beneficial in identifying faults that were previously challenging to detect through geological methods alone. The major faults of Brevard (northern section), Towaliga-Lowndesville (central piedmont), and Bartletts Ferry (near the FL) are indicated on the geological map (Fig. 8).

Fig. 9a shows the aeromagnetic data of the study area. The data were RTP as shown in Fig. 9b. To reduce noise and produce smoother edge determination maps, the αVGR stable filter was applied to the RTP anomaly maps before computing the edge determination filters.

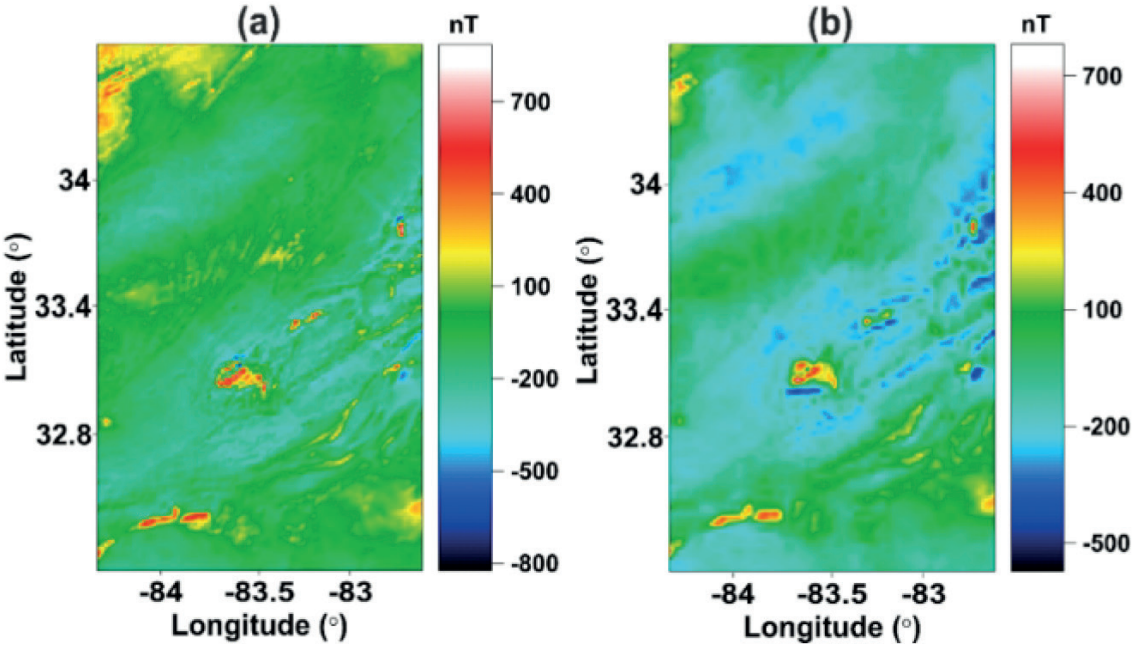

Fig. 9 - a) Aeromagnetic anomaly; b) RTP aeromagnetic anomaly of the Georgia area, USA.

Fig. 10a illustrates the *THG* map of the aeromagnetic anomaly identified in the RTP data set. The *THG* displays significant anomalies with high amplitudes, complicating the creation of a definitive structural map of Georgia. Fig. 10b presents the edge image created by the *TA* detector. Although this method provides a well-balanced representation of the magnetic sources, it also results in extracted structures that lack sharpness. Fig. 10c, similarly to the synthetic cases, fails to present a balanced representation of the distribution of various sources in Georgia. Fig. 10d shows the outcome of the *TDX*. While the *TDX* is more effective in generating distinct edge images compared to the *THG*, *TA*, and *THGTA*, the source edges appear to be interconnected. Figs. 10e and 10f show the results of edge detection using the *HTA* and *ITHG* filters, respectively; however, neither method delineates all the edges effectively. Fig. 10g displays the image map from the *TATHG* algorithm, which successfully identifies the source edges; however, it exhibits indistinct boundaries and low resolution (Alvandi and Ardestani, 2023; Ai *et al.*, 2024a). The boundaries defined by the *THGMTH* are shown in Fig. 10h. Although this detector produces high-resolution structural images, it tends to introduce spurious edges around the sources. Figs. 10i, 10j, and 10k illustrate the results obtained from the *GF* filter with varying *M* values, where

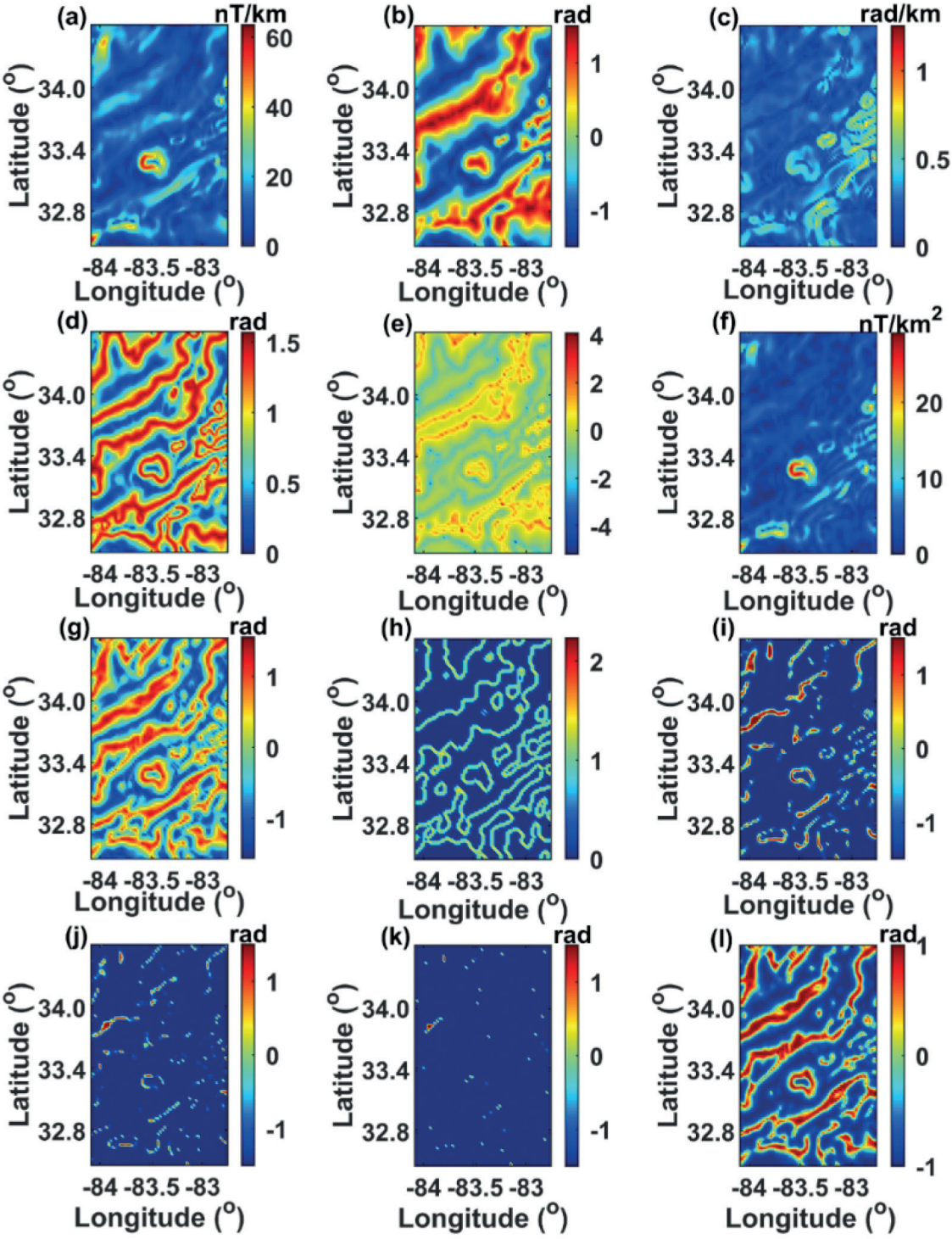

Fig. 10 - Horizontal boundary determination maps of data in Fig. 9b: a) *THG*; b) *TA*; c) *THGTA*; d) *TDX*; e) *HTA*; f) *ITHG*; g) *TATHG*; h) *THGMTH*; i) *GF* (*M*=0.5); j) *GF* (*M*=1.5); k) *GF* (*M*=8); and l) *MGTHG*.

the delineation of the boundaries of buried structures appears blurred and indistinct. Ultimately, Fig. 10l depicts the edges identified by the *MGTHG*. This proposed methodology demonstrates superior resolution in delineating edges when compared to other techniques.

7. The αVGR-tilt-depth technique

Estimating the depth of magnetic and gravity sources is a critical component of structural geology. Accurate depth estimation and edge enhancement significantly improve the understanding of the spatial distribution of geological structures within a given area (Alvandi and Ghanati, 2023). One widely used technique for determining the position and depth of these sources is the tilt-depth (TD) method. This method provides valuable insights into the geological framework by precisely identifying the depth and location of subsurface features, thereby, enabling more informed interpretations and decisions in geological studies (Salem *et al.*, 2008). In this study, the αVGR-TD (αVGTD) method, a recent modification of the TD technique, has been employed (Abdelrahman *et al.*, 2024). The αVGR technique, as outlined in Eq. (16), is utilised to calculate the vertical gradient in the TD technique. Fig. 11a showcases the solutions generated by the αVGTD method applied to the study area, highlighting a strong correlation with the lineaments identified using the *MGTHG* filter. The histogram in Fig. 11b illustrates the variations in estimated depths, which range from 1 to 9.5 km, with an average depth of 4.30 km. The highest frequency of depth estimates occurs within the 3- to 5.5-kilometre interval.

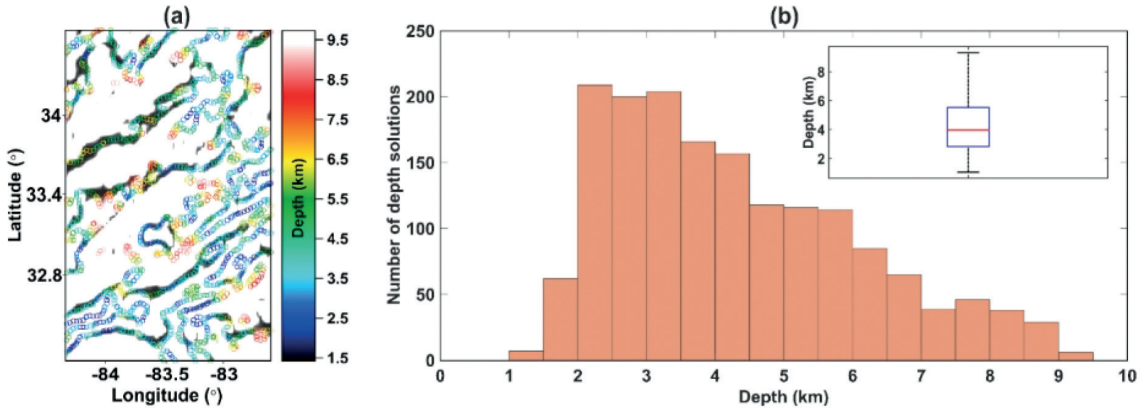

Fig. 11 - a) Description of the location and depth of magnetic sources obtained through the αVGTD method; b) histogram illustrating the frequency distribution of αVGTD solutions.

8. Conclusions

The precise interpretation of subsurface structures heavily relies on the accurate recognition of horizontal boundaries. This process has been significantly improved through noise reduction, leading to the increased use of innovative filtering techniques. Edge enhancement filters, which detect anomalies via derivatives, have gained popularity despite their tendency to amplify noise within the data set. The *MGTHG* filters, when combined with vertical gradients calculated using the αVGR method, exhibit superior performance in amplifying both weak and strong signals

simultaneously. This enhancement is achieved without introducing extraneous information into the edge map. The application of the *MGTHG* filter has led to the generation of a distinct structural map for a region in Georgia, USA, providing valuable insights for establishing a novel structural and tectonic framework. This filter is characterised by its high resolution, ability to eliminate false edges, and capacity to reveal subtle geological features.

Acknowledgments. We would like to express our sincere gratitude to Antonella Peresan, Valeria Paoletti, and the esteemed reviewers for their invaluable support to this research. Additionally, we wish to extend our appreciation to the United States Geological Survey (USGS) for granting permission to use the geological map and aeromagnetic data presented in Figs. 8 and 9a. The data were retrieved from https://www.usgs.gov on 20 May 2024.

REFERENCES

Abdelrahman K., Pham L.T., Oliveira S.P., Duong V.H., Kieu T.D., Gomez-Ortiz D., Fnais M.S. and Eldosouky A.M.; 2024: *Reliable Tilt-depth estimates based on the stable computation of the tilt angle using robust vertical derivatives.* Sci. Rep., 14, 7392, doi: 10.1038/s41598-024-57314-5.

Ai H., Deniz Toktay H., Alvandi A., Pasteka R., Su K. and Liu Q.; 2024a: *Advancing potential field data analysis: the Modified Horizontal Gradient Amplitude method (MHGA)*. Contribut. Geophys. Geod., 54, 119-143, doi: 10.31577/congeo.2024.54.2.1.

Ai H.E., Ekinci Y.L., Alvandi A., Deniz Toktay H., Balkaya Ç. and Roy A.; 2024b: *Detecting edges of geologic sources from gravity or magnetic anomalies through a novel algorithm based on hyperbolic tangent function*. Turkish J. Earth Sci., 33, 6, doi: 10.55730/1300-0985.1936.

Al-Bahadily H.A., Al-Rahim A.M. and Smith R.S.; 2023: *Determination of reactivated regions and faults in the Iraq southern Desert with the new edge technique, Inverse Tilt Angle of Second-gradients (ITAS)*. Acta Geophys., 72, 1675-1692.

Alarifi S.S.; 2022: *Structural implications of potential field data on southeastern North America*. J. Geophys. Eng., 19, 142-156, doi: 10.1093/jge/gxac005.

Alvandi A. and Ardestani V.E.; 2023: *Edge detection of potential field anomalies using the Gompertz function as a high-resolution edge enhancement filter*. Bull. Geophys. Ocean., 64, 279-300.

Alvandi A. and Ghanati R.; 2023: *Using magnetic data for estimating the location of lateral boundaries and the depth of the shallow salt dome of Aji-Chai, east Azerbaijan province, Iran*. Int. J. Min. Geo-Eng., 57, 251-258, doi: 10.22059/ijmge.2023.352685.595014.

Alvandi A. and Motavalli-Anbaran S.H.; 2024: *Detection of the horizontal boundary of gravity anomalies using the hybrid positive and negative curvature (PNH) procedure*. J. Earth Space Phys., 50, 323-340, doi: 10.22059/jesphys.2024.362046.1007541.

Alvandi A., Deniz Toktay H. and Nasri S.; 2022a: *Application of direct source parameter imaging (direct local wave number) technique to the 2D gravity anomalies for depth determination of some geological structures.* Acta Geophys., 70, 659-667, doi: 10.1007/s11600-022-00750-6.

Alvandi A., Toktay H.D. and Pham L.T.; 2022b: *Capability of improved logistics filter in determining horizontal boundaries and edges of gravity and magnetic anomalies Tuzgolu area, Turkey*. J. Min. Eng., 17, 57-72.

Alvandi A., Su K., Ai H., Ardestani V.E. and Lyu C.; 2023a: *Enhancement of potential field source boundaries using the hyperbolic domain (Gudermannian function)*. Miner., 13, 1312, doi: 10.3390/min13101312.

Alvandi A., Toktay H. and Ardestani V.E.; 2023b: *Edge detection of geological structures based on a logistic function: a case study for gravity data of the western Carpathians.* Int. J. Min. Geo-Eng., 57, 267-274, doi: 10.22059/ijmge.2023.353516.595018.

Bentley R.O., Higgins M.W., Pickering S.M., Grant W.H., Zietz I. and Neathery T.L.; 1974: *Preliminary interpretation of an aeromagnetic map of most of the central and southern Georgia Piedmont.* Geol. Soc. Am. Abstr. with Programs, 6, 333-334.

Cooper G.R.J.; 2020: *A modified enhanced horizontal derivative filter for potential field data*. Explor. Geophys., 51, 549-554.

Cooper G.R.J. and Cowan D.R.; 2006: *Enhancing potential field data using filters based on the local phase*. Comput. Geosci., 32, 1585-1591.

Cordell L. and Grauch V.J.S.; 1985: *Mapping basement magnetization zones from aeromagnetic data in the San Juan basin, New Mexico*. In: Hinze W.J. (ed), The utility of regional gravity and magnetic maps. Publ. Soc. Explor. Geophys., 181-197, doi: 10.1190/1.0931830346.ch16.

Daniels D.L.; 1974: *Geologic interpretation of geophysical maps, central Savannah River area, South Carolina and Georgia - Map GP-893.* Department of the Interior, U.S. Geological Survey, Geophysical Investigations, Reston, VA, USA, 10 pp., doi: 10.3133/gp893.

Daniels D.L.; 2001: *Georgia aeromagnetic and gravity maps and data: a web site for distribution of data.* U.S Geological Survey, Reston, VA, USA, Open-File Report 2001-106, doi: 10.3133/ofr01106.

Deniz Toktay H., Aydogan D. and Yüksel F.; 2021a: *Quantitative analysis of total magnetic anomaly maps on archaeological sites - Part 1.* Math. Methods Appl. Sci., 44, 13696-13710.

Deniz Toktay H., Aydogan D. and Yüksel F.; 2021b: *Quantitative analysis of total magnetic anomaly maps on archaeological sites - Part 2.* Math. Methods Appl. Sci., 44, 13684-13695.

Deniz Toktay H., Prasad K.N.D. and Alvandi A.; 2024: *Edge enhancement of potential field data using the Enhanced Gradient (EG) filter.* Bull. Miner. Res. Explor., 174, 55-66, doi: 10.19111/bulletinofmre.1386653.

Ekinci Y.L. and Yigitbas E.; 2015: *Interpretation of gravity anomalies to delineate some structural features of the Biga and Gelibolu peninsulas and their surroundings (northwest Turkey)*. Geodinamica Acta, 27, 300-319, doi: 10.1080/09853111.2015.1046354.

Ekinci Y.L., Ertekin C. and Yigitbas E.; 2013: *On the effectiveness of directional derivative based filters on gravity anomalies for source edge approximation: synthetic simulations and a case study from the Aegean graben system (western Anatolia, Turkey).* J. Geophys. Eng., 10, 035005.

Ekinci Y.L., Buyuksarac A., Bektas O. and Ertekin C.; 2020: *Geophysical investigation of Mount Nemrut Stratovolcano (Bitlis, eastern Turkey) through aeromagnetic anomaly analyses.* Pure Appl. Geophys, 177, 3243-3264, doi: 10.1007/s00024-020-02432-0.

Eldosouky A.M., El-Qassas R.A.Y., Pour A.B., Mohamed H. and Sekandari M.; 2021: *Integration of ASTER satellite imagery and 3D inversion of aeromagnetic data for deep mineral exploration*. Adv. Space Res., 68, 3641-3662.

Eldosouky A.M., Pham L.T. and Henaish A.; 2022: *High precision structural mapping using edge filters of potential field and remote sensing data: a case study from Wadi Umm Ghalqa area, south eastern Desert*, Egypt. Egypt. J. Remote Sens. Space Sci., 25, 501-513, doi: 10.1016/j.ejrs.2022.03.001.

Fedi M. and Florio G.; 2001: *Detection of potential fields source boundaries by enhanced horizontal derivative method.* Geophys. Prospect., 49, 40-58.

Ferreira F.J.F., de Souza J., Bongiolo A.B.S. and de Castro L.G.; 2013: *Enhancement of the total horizontal gradient of magnetic anomalies using the tilt angle*. Geophys., 78, J33-J41.

Hack J.T.; 1982: *Physiographic divisions and differential uplift in the Piedmont and Blue Ridge.* U.S. Department of the Interior, Geological Survey, Washington, DC, USA, Geological Survey professional paper, 1265, 55 pp.

Ibraheem I.M., Tezkan B., Ghazala H. and Othman A.A.; 2023: *A new edge enhancement filter for the interpretation of magnetic field data.* Pure Appl. Geophys., 180, 2223-2240.

Lawton D.E., Moye F.J., Murray J.B., O'Connor B.J., Penley H.M., Sandrock G.S., Marsalis W.E., Friddell M.S., Hetrick J.H., Huddlestun P.F., Hunter R.E., Mann W.R., Martin B.F., Pickering S.M., Schneeberger F.J. and Wilson J.D.; 1976: *Geologic map of Georgia*, *Scale 1:500,000.* Georgia Department of Natural Resources, Geologic and Water Resources Division, Georgia Geological Survey, Atlanta, GA, USA.

Miller H.G. and Singh V.; 1994: *Potential field tilt a new concept for location of potential field sources*. J. Appl. Geophys., 32, 213-217, doi: 10.1016/0926-9851(94)90022-1.

Nabighian M.N.; 1984: *Towards a three-dimensional automatic interpretation of potential field data via generalized Hilbert Transforms; fundamental relations*. Geophys., 49, 780-786, doi: 10.1190/1.1441706.

Narayan S., Kumar U., Pal S.K. and Sahoo S.D.; 2021: *New insights into the structural and tectonic settings of the Bay of Bengal using high-resolution earth gravity model data.* Acta Geophys., 69, 2011-2033.

Nayak A.K. and Pal A.; 2019: *Development and validation of an adsorption kinetic model at solid-liquid interface using normalized Gudermannian function.* J. Mol. Liq., 276, 67-77.

Oliveira S.P. and Pham L.T.; 2022: *A stable finite difference method based on upward continuation to evaluate vertical derivatives of potential field data.* Pure Appl. Geophys., 179, 4555-4566.

Pal S.K., Majumdar T.J., Pathak V.K., Narayan S., Kumar U. and Goswami O.P.; 2016: *Utilization of high-resolution EGM2008 gravity data for geological exploration over the Singhbhum-Orissa Craton, India*. Geocarto Int., 31, 783-802, doi: 10.1080/10106049.2015.1076064.

Pham L.T.; 2023: *A novel approach for enhancing potential fields: application to aeromagnetic data of the Tuangiao, Vietnam.* Eur. Phys. J. Plus., 138, 1134, doi: 10.1140/epjp/s13360-023-04760-1.

Pham L.T. and Prasad K.N.D.; 2023: *Analysis of gravity data for extracting structural features of the northern region of the central Indian Ridge.* Vietnam J. Earth Sci., 45, 147-163, doi: 10.15625/2615-9783/18206.

Pham L.T., Oksum E. and Eldosouky A.M.; 2023: *High precision subsurface structural mapping of the Trompsburg complex (South Africa) from gravity and magnetic data*. Adv. Space Res., 71, 2348-2356.

Pickering S.M. and Murray J.B.; 1976: *Geologic map of Georgia, scale 1:500,000*. Georgia Department of Natural Resources, Geologic and Water Resources Division, Georgia Geological Survey, Atlanta, GA, USA.

Prasad K.N.D., Pham L.T. and Singh A.P.; 2022a: *A novel filter "ImpTAHG" for edge detection and a case study from Cambay Rift basin, India.* Pure Appl. Geophys., 179, 2351-2364.

Prasad K.N.D., Pham L.T. and Singh A.P.; 2022b: *Structural mapping of potential field sources using BHG filter.* Geocarto Int., 37, 11253-11280.

Prasad K.N.D., Pham L.T., Singh A.P., Eldosouky A.M., Abdelrahman K., Fnais M.S. and Gómez-Ortiz D.; 2022c: *A novel Enhanced Total Gradient (ETG) for interpretation of magnetic data*. Miner., 12, 1468, doi: 10.3390/min12111468.

Rao D.B. and Babu N.R.; 1991: *A rapid method for three-dimensional modeling of magnetic anomalies*. Geophys., 56, 1729-1737.

Rao D.B., Prakash M.J. and Babu N.R.; 1990: *3-D and 2 1/2-D modeling of gravity anomalies with variable density contrast.* Geophys. Prospect., 38, 411-422.

Roest W.R., Verhoef J. and Pilkington M.; 1992: *Magnetic interpretation using the 3-D analytic signal.* Geophys., 57, 116-125.

Sahoo S.D., Narayan S. and Pal S.K.; 2022: *Fractal analysis of lineaments using CryoSat-2 and Jason-1 satellite-derived gravity data: evidence of a uniform tectonic activity over the middle part of the central Indian Ridge.* Phys. Chem. Earth, Parts A/B/C, 128, 103237, doi: 10.1016/j.pce.2022.103237.

Saibi H., Aboud E. and Ehara S.; 2012: *Analysis and interpretation of gravity data from the Aluto-Langano geothermal field of Ethiopia.* Acta Geophys., 60, 318-336.

Saibi H., Amir G. and Mohamed F.S.; 2019: *Subsurface structural mapping using gravity data of AlAin region, Abu Dhabi Emirate*. United Arab Emirates Geophys. J. Int., 216, 1201-1213.

Salem A., Williams S., Fairhead D., Smith R. and Ravat D.; 2008: *Interpretation of magnetic data using tilt-angle derivatives.* Geophys., 73, L1-L10.

Tatchum N.C., Tabod C., Koumetio F. and Manguelle-Dicoum E.; 2011: *A gravity model study for differentiating vertical and dipping geological contacts with application to a Bouguer gravity anomaly over the Foumban shear zone, Cameroon.* Geophys., 47, 43-55.

Verduzco B., Fairhead J.D., Green C.M. and MacKenzie C.; 2004: *New insights into magnetic derivatives for structural mapping.* Lead. Edge, 23, 116-119.

Corresponding author: Seyed-Hani Motavalli-Anbaran
Institute of Geophysics, University of Tehran
North Kargar Ave., Tehran, Iran
Phone: +98 21 6111 8315; e-mail: motavalli@ut.ac.ir